Geochemistry Geophysics Geosystems G3

*Article*
Volume 14, Number 8
28 August 2013
doi: 10.1002/ggge.20185
ISSN: 1525-2027

Published by AGU and the Geochemical Society

# Study of the western edge of the African Large Low Shear Velocity Province

**Daoyuan Sun and Meghan S. Miller**

*Department of Earth Sciences, University of Southern California, ZHS, 3651 Trousdale Pkwy, Los Angeles, California, 90089, USA (daoyuans@usc.edu)*

[1] It is well established that there is a large low shear velocity province (LLSVP) in the lowermost mantle beneath Africa, extending from beneath the southeastern Atlantic Ocean to the southwestern Indian Ocean. The detailed 3-D geometry of the LLSVP is crucial to the understanding of how this prominent lower mantle feature developed and evolved. Most studies have concentrated on mapping the southern and eastern edges of African LLSVP using the Kaapvaal array at South Africa. Here we use data from recently deployed arrays in the western Mediterranean to study its northwestern edge and evaluate the sharpness of its boundaries. Travel time and waveform modeling of S and SKS phases suggest the existence of sharp low velocity anomalies in the lowermost mantle beneath the eastern Atlantic Ocean, which agrees with global tomography models. However, the S-SKS differential times vary up to 6 s across the array. To match the large travel time variations and waveforms, the existence of a slow velocity structure with a sharp top is required. The structure has a 3.5% reduction in shear wave velocity and a height of ~600 km above the core-mantle boundary, which is lower in topography than the southern and eastern part of the African LLSVP. Further 3-D synthetic waveforms and modeling calculations demonstrate the existence of these sharp boundaries for the northwestern portion of the African LLSVP. The strong lateral variation in both travel times and waveforms suggests that this part of the African LLSVP may be as complex as the mid-Pacific LLSVP. To explain the observed sharp top and large dome-like structure, a thermochemical origin of the African LLSVP is supported.

**Components:** 43,161 words, 15 figures, 1 table.

**Keywords:** African LLSVP; sharp top; thermochemical.

**Index Terms:** 7200 Seismology; 7208 Mantle; 7207 Core; 7203 Body waves; 1200 Geodesy and Gravity; 1213 Earth's interior: dynamics; 1212 Earth's interior: composition and state; 1500 Geomagnetism and Paleomagnetism; 1507 Core processes; 8100 Tectonophysics; 8120 Dynamics of lithosphere and mantle: general; 8115 Core processes; 8124 Earth's interior: composition and state.

**Received** 18 February 2013; **Revised** 20 May 2013; **Accepted** 24 May 2013; **Published** 28 August 2013.

Sun, D., and M. S. Miller (2013), Study of the western edge of the African Large Low Shear Velocity Province, *Geochem. Geophys. Geosyst., 14*, 3109–3125, doi:10.1002/ggge.20185.

## 1. Introduction

[2] The Large Low Shear Velocity Provinces (LLSVPs) beneath Africa and the mid-Pacific are two dominant features in lower mantle tomography models. With recent developments of inversion techniques and dense seismic arrays, images of the two LLSVPs have been greatly improved [*Grand*, 2002; *Masters et al*., 2000; *Montelli et al*., 2006; *Ritsema et al*., 2011; *Ritsema et al*., 2004; *Simmons et al*., 2010, 2007; *Su and Dziewonski*, 1997]. The two LLSVPs display common

degree two features: positive density perturbations of a few percent, and anticorrelated bulk sound velocity and shear velocity inside the structure [*Ishii and Tromp*, 1999; *Masters et al*., 2000]. However, their interior structure at smaller scales appear to differ, with the Pacific anomaly including several separated piles compared to the evidently monolithic African anomaly [*He and Wen*, 2012; *Helmberger and Ni*, 2005; *Liu et al*., 2011].

[3] Extensive studies have been done on the African LLSVP, which extends from beneath the southeastern Atlantic Ocean to the southwestern Indian Ocean [*Ritsema et al*., 1998; *To et al*., 2005; *Wang and Wen*, 2007]. It has a dome-like structure with dimensions of about 1200 km wide and up to 1000 km high [*Helmberger and Ni*, 2005]. Inside the African LLSVP, the shear velocity perturbation is about −3% and the compressional velocity perturbation is negligible. Studies of rapid variations of travel times and anomaly waveforms concluded that sharp sides exist at the south and east of the African LLSVP [*Ni and Helmberger*, 2003a, 2003b, 2003c; *Ni et al*., 2002]. When rays travel along sharp-sided structures, such as the vertical "wall structure" of southern African LLSVP [*Sun et al*., 2009], strong 3-D waveform distortion effects are observed. However, most previous studies have utilized on 2-D simulations, and only recently advances in computational seismology have made full 3-D waveform modeling possible [*Ni et al*., 2005; *To et al*., 2005].

[4] It has been proposed that the long wavelength heterogeneity of the LLSVPs may be dominated by thermal effects [*Davies et al*., 2012; *Simmons et al*., 2009], but purely thermal models have difficulty in satisfying observed structural characteristics of the LLSVP: high elevation, long-term stability, sharp vertical sides, and in particular, the large-scale dome-like shape. Therefore, introducing chemical heterogeneities into the LLSVPs are required to match the seismic observations and many thermochemical models have been developed to explain their origin and structure [*Bower et al*., 2013; *McNamara and Zhong*, 2004, 2005; *Tackley*, 2012; *Tan and Gurnis*, 2005, 2007]. To produce piles instead of ridge-like features, a much higher intrinsic viscosity within the LLSVP is needed. For example, *Tan and Gurnis* [2005] produced a model with a large bulk modulus to explain the anticorrelation between the bulk sound velocity and shear velocity, at the same time and those observed sharp travel time anomalies [*Sun et al*., 2007]. Furthermore, the detailed morphology of the LLSVP is also largely controlled by the plate motion history as they are influenced by the position of slab structures as they enter the lower mantle [*Bower et al*., 2013; *Zhang et al*., 2010].

[5] The detailed 3-D nature of the African LLSVP is the key to developing a more realistic thermochemical convection model, especially to satisfy the known volumetric information from seismological constraints. However, our understanding of the African LLSVP is almost exclusively based on studies of its southern and eastern boundaries. We have been missing the detailed properties of its northwestern boundary. Where do the boundaries extend to the north and west? Do similar sharp sides also exist at these boundaries? Is there an even average height across the lateral extent of the African LLSVP?

[6] In this paper, we use waveforms recorded by the PICASSO array and other regional arrays in the westernmost Mediterranean to study the multipathing effects along the northwestern boundary of the African LLSVP. Additional 3-D waveform modeling presents evidence that a sharp boundary exists at the northwestern edge of the African LLSVP, which further argues in favor of a thermochemical origin of the African LLSVP.

## 2. Data and Multipathing Maps

### 2.1. Data

[7] The PICASSO Array was deployed for a multidisciplinary effort to understand the geodynamics of the westernmost margin of the Mediterranean (Figure 1). Combining the PICASSO array with IberArray, Munster Morocco Array, CoMITAC (Morocco-Bristol Network), and French and Portuguese regional arrays, provides more than 120 stations in this area. The position of the array relative to the South Sandwich Islands allows for using multiple phases to analyze the lowermost mantle structure of the western edge of the African LLSVP (Figure 2).

[8] We use six events (A through F) that occurred between 2011 and 2012 (Table 1 and Figure 1b) within the distance range of 85–105° for analysis of phases S, ScS, and SKS (Figure 2). The locations of the events, magnitude, and mechanisms were determined by the Harvard Centroid Moment Tensor solutions [*Dziewonski et al*., 1981]. The instrument responses were deconvolved from the seismograms and a bandpass filter

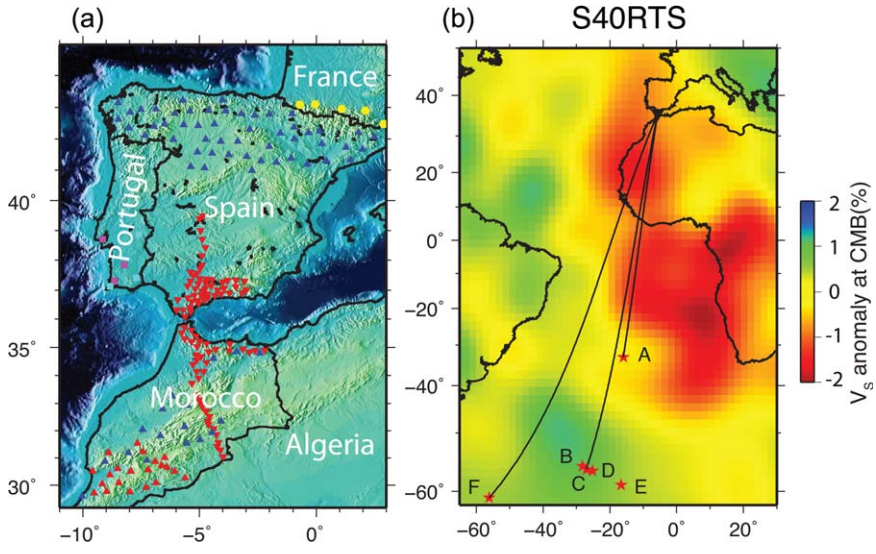


**Figure 1.** (a) Location map of broadband seismic stations used in this study. Red inverted triangles denote the PICASSO array. Blue triangles denote stations from the IberArray. The orange triangles are CoMITAC array and Munster-Morocco array. Yellow circles are stations of French Broadband Seismological Network. Red and green squares are stations denote LX and PM stations at Portugal. (b) The locations of the events used here (red stars) and the great circle paths to the array are depicted by black lines. The tomographic model S40RTS [*Ritsema et al.*, 2011] is plotted for the bottom of the mantle. Note the rays sample the western edge of LLSVP in the tomographic models.

(3–50 s) was applied before rotation into the tangential (SH) and radial (SV) components of displacement.

[9] The ray paths for the Sandwich Island events (events B, C, D, and E) to the stations cross the western boundary of the African LLSVP as imaged in the lower mantle tomography model by *Ritsema et al.* [2011] (Figures1b and 2a; Figure S1, supporting information).[1] For the westernmost stations, the S phases sample a region without significant shear wave velocity perturbation, which is similar to preliminary reference Earth model (PREM) [*Dziewonski and Anderson*, 1981] in the lowermost mantle (Figure 1b), however the S phases recorded at the stations on the eastern side of the array are expected to sample the inside of the African LLSVP. This combination of events and stations provide an ideal opportunity to study the multipathing effects related to the sharp boundaries. For comparison, the event F samples the lower mantle further to the west (Figure 1b), which is important for defining the western boundary of the African LLSVP. We also included a shallow mid-Atlantic Ridge event (event A), as its ScS travel times provide constraints on the shear velocity perturbation inside the African LLSVP.

## 2.2. Methodology

[10] By examining the coherent multipathing signatures across a seismic array, *Sun et al.* [2009] developed a Multipathing Detector (MPD) to map sharp structures in the deep Earth. With recently increasing volume of array data, this method allows for study of waveforms in a more systematical manner. The method simulates each observed body waveform D(t) by performing a decomposition with $[S(t) + C \times S(t - \Delta_{LR})]/2$, where S(t) is the synthetic for a reference model with a simple pulse shape. Time separation ($\Delta_{LR}$) and amplitude ratio (C) are determined by obtaining a high cross correlation between a simulated waveform and the data found by a simulated annealing method. The travel time of the composite waveform relative to the reference model synthetic is then defined as $\Delta_T$ (Figure 3a). Whereas conventional tomography yields a travel time correction ($\Delta_T$), it introduces large errors when cross-correlating synthetics with strongly distorted waveforms directly. In addition to accurate travel time measurements ($\Delta_T$), it yields an extra parameter, $\Delta_{LR}$, which describes the waveform complexity [*Sun and Helmberger*, 2011; *Sun et al.*, 2009]. Larger

[1]All supporting information may be found in the online version of this article.

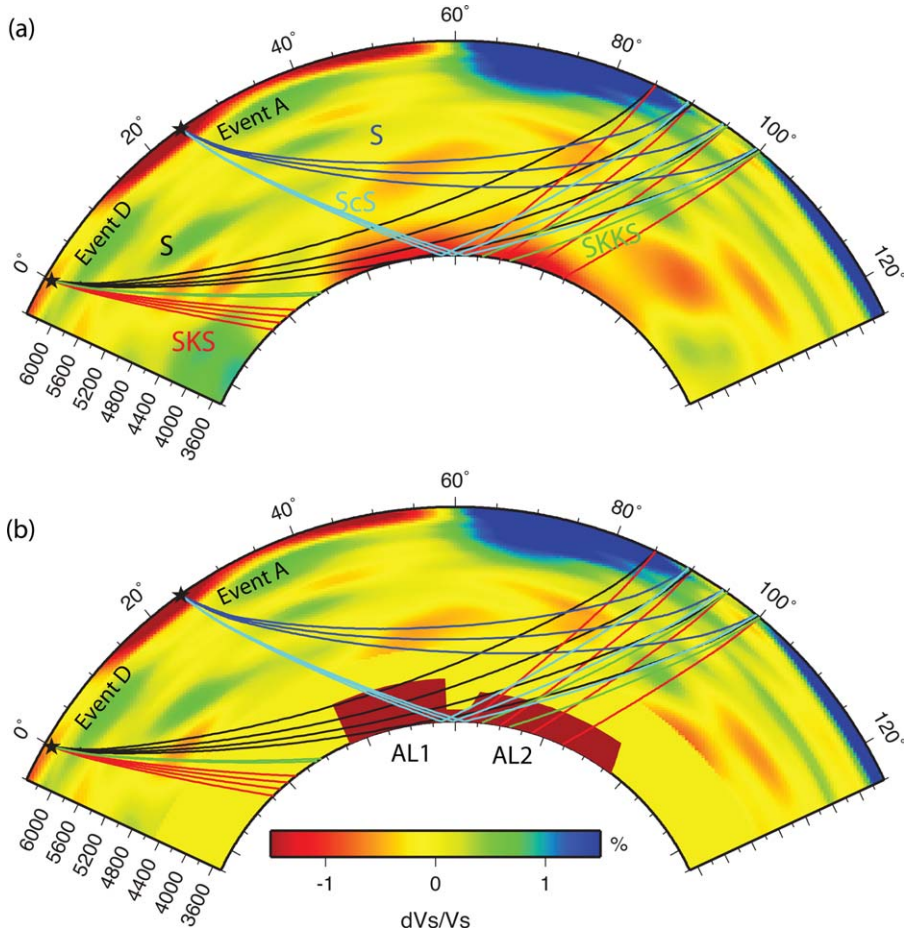


**Figure 2.** 2-D cross sections along the great circle path in Figure 1b of (a) S40RTS [*Ritsema et al*., 2011] and (b) our preferred model SMWA. Ray paths of S (blue for event A, black for event C), SKS (red), SKKS (green), and ScS (cyan) used in this study are also displayed. In model SMWA, the shear velocity perturbations inside both south (AL1) and north (AL2) portions are uniform−3.5%.

values of $\Delta_{LR}$ denote stronger mutlipathing and more distorted waveforms. Two examples of the waveforms are displayed in Figure 3a. Station PM02 has characteristically simple waveforms, which corresponds to a small value of $\Delta_{LR}$. In contrast, station PS21 has complicated waveforms, which produces large values of $\Delta_{LR}$.

[11] By utilizing arrays we can construct maps of $\Delta_{LR}$ values to describe the sharp structures directly [*Sun et al*., 2009]. For example, a horizontal structure will introduce waveform complexity with epicentral distance changing, which is called in-plane multipathing. In contrast, an azimuthally orientated $\Delta_{LR}$ pattern indicates a vertical structure with out-of-plane multipathing. Using such maps, we can easily recognize features with high- or low-velocity anomalies and define their sharp edges. MPD techniques have been successfully applied to several situations: the sharp side of the southwestern African LLSVP, detection of a mid-mantle plume [*Sun et al*., 2010], and sharp structures in the upper mantle [*Chu et al*., 2012; *Sun and Helmberger*, 2011]. Here we apply MPD on both S and SKS phases.

**Table 1.** Earthquakes Used in This Study

| Event | Date | Latitude (deg.) | Longitude (deg.) | Depth (km) |
|---|---|---|---|---|
| A | 22 Mar 2011 | −33.10 | −15.98 | 10 |
| B | 11 Dec 2011 | −56.01 | −28.18 | 116 |
| C | 3 Sep 2011 | −56.55 | −27.04 | 106 |
| D | 22 Jan 2012 | −56.76 | −25.15 | 13 |
| E | 17 Apr 2012 | −59.01 | −16.62 | 12 |
| F | 15 Jan 2012 | −60.95 | −56.11 | 8 |

[12] Furthermore, we use a recently developed staggered grid Finite Difference code (D. Li et al., Modeling global seismograms using 2D finite difference method, submitted to Geophys. J. Int., 2013) to develop the preferred model SMWA (Figure 2b) for the western African LLSVP by

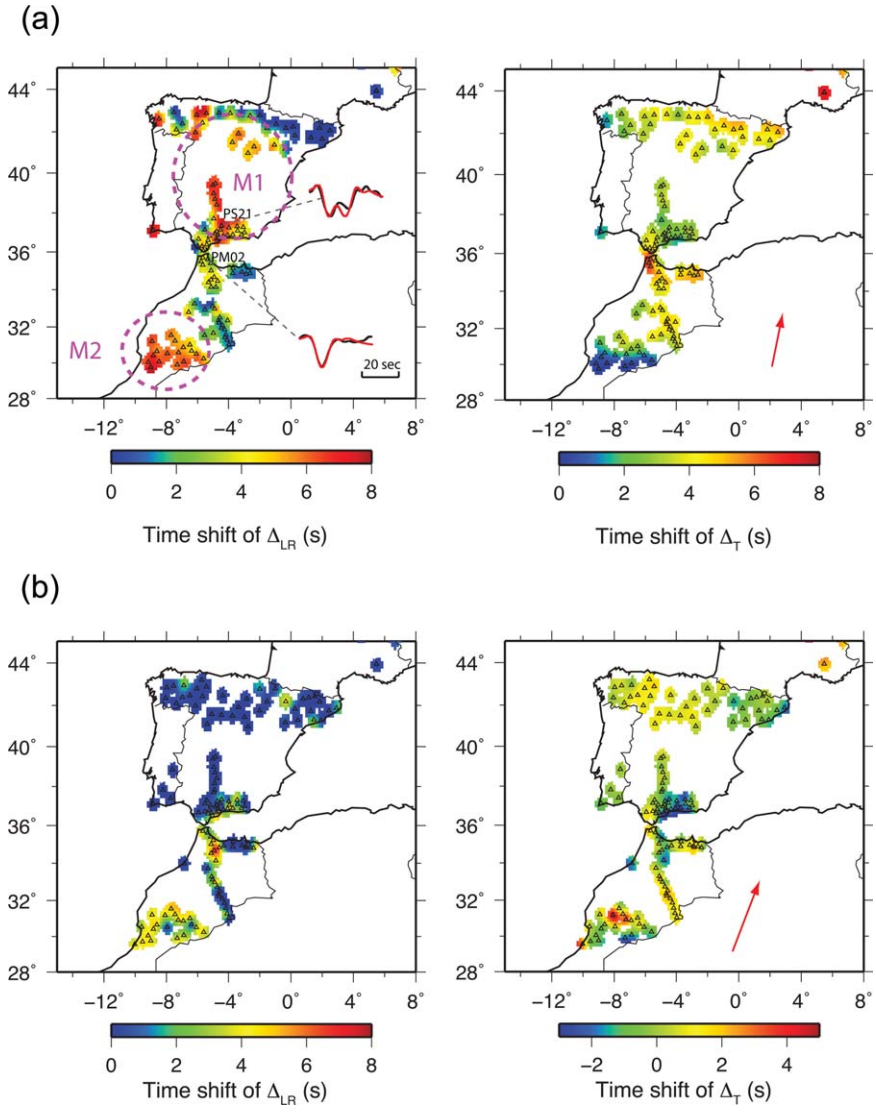


**Figure 3.** MPD patterns on the SH component for (a) event B and (b) event F (Figure 1b). In Figure 3a, examples of MPD simulations (red) and data (black) waveforms for stations PICASSO stations PM02 and PS21 are displayed. The record of PS21 has double arrivals, which produce large $\Delta_{LR}$ values (indicated by reds). The red arrow indicates the average direction of ray paths to the array.

fitting both travel times and waveform data that is presented here. The model SMWA has two subregions: AL1 (southern portion) and AL2 (northern portion), where the AL1 portion of the model has a height of 600 km and AL2 is constrained to 400 km height above the CMB. The constraints on the model properties are discussed in detail later.

## 3. Results

### 3.1. Waveform Complexity

[13] For the South Sandwich Island event B, strong multipathing up to ~7 s on the S phases (indicated by red colors) are observed by the stations in central to northern Spain, circled area M1 (Figure 3a). The stations in southern Morocco, circled area M2, display moderate multipathing with $\Delta_{LR}$ values up to ~5 s. For event F (Figure 3b), the $\Delta_T$ patterns are similar to those for event B. However, the $\Delta_{LR}$ values are smaller indicating reduced multipathing effects. Although the raypaths for event F sample the African LLSVP further to the west (Figure 1b), the backazimuth range is similar to event B. If the observed strong multipathing features for the event B are caused by the receiver-side anomalous structures in the upper mantle or crust, the structures will also affect the event F, which is not the case here.

Therefore, the different multipathing patterns between the two events demonstrate the sharpness of the western boundary of the African LLSVP, which is only sampled by event B.

[14] Due to radiation pattern complications, we do not have good S records on both the tangential (SH) and radial (SV) components for the same events. However, the Sandwich Island events chosen (events B, C, and D) are closely spaced and can provide complementary multipathing patterns for both the SH and SV components (Figure S2, supporting information). Figure 4a shows an example of MPD patterns for the SKS phase for the deep event C, which has no obvious multipathing across the entire array except in the central Betics of southernmost Spain and three stations in Morocco. The SV MPD patterns for deep event C are shown in Figure 4b, which indicates strong multipathing (large $\Delta_T$, yellow and red colors) in central to northern Spain. The values of $\Delta_{LR}$ are comparable with those observed for the SH components for event B (circled area M1 in Figure 3a). In contrast, the western stations in Figures 3a and 4b display less multipathing effects. This azimuthal variation in the multipathing patterns suggests that a sharp structural boundary exists in between the region where the ray paths arrival in central Spain and Portugal from the south with a near north-south orientation. The ray paths for SKS and S (as seen in Figure 2) are very similar in the upper mantle, therefore the strong multipathing observed in the S waveforms must be caused by structures in the lower mantle. In addition, this strong multipathing pattern associated with delayed arrivals verifies that the structure is a slow anomaly, as expected for the position of the African LLSVP.

[15] We do observe differences in the MPD patterns for SV and SH. The SV $\Delta_{LR}$values for the stations in southern Morocco are less strong than those on the SH component, which we attribute to the interference of SKS and ScS on SV at this distance (87∼90°). The similar patterns for both shallow (Figure S2) and deep events further confirm that those apparent sharp anomalies are not due to source side structures. The lateral variations in the $\Delta_{LR's}$ patterns of the event B also indicate the boundary having a preferred orientation. In short, we conclude that the strong multipathing effects observed in the S waveform data appear to be caused by African LLSVP.

[16] We expect sharp upper mantle structures to promote multipathing effects for S and SKS in the same manner. This is evident in the data from stations in the Betics of southern Spain (Figure 4). For those stations, both S and SKS show large $\Delta_{LR}$ values (red color) and earlier arrivals (smaller $\Delta_T$), which suggests the presence of a fast sharp anomaly in the upper mantle. This is further supported by regional body wave and surface tomographic models [*Bezada et al*., 2013; *Marone et al*., 2004; *Yang et al*., 2007; *Zhu et al*., 2012; (I. Palomeras et al., Finite-Frequency Rayleigh Wave tomography of the Western Mediterranean, submitted to Geochem. Geophys. Geosyst., 2013)]. Beneath Southern Spain, the Alboran slab is clearly imaged as a localized high-velocity structure in the upper mantle in the tomography models. However, the multipathing effects from the upper mantle are very small (200 km × 100 km, magenta rectangle area in Figure 4) for most stations as shown in the SKS patterns in Figure 4a, so here we will concentrate on how the lower mantle African LLSVP affects the S waveforms.

### 3.2. Travel Time Measurements

[17] Travel time measurements, $\Delta_T$, for the S and SKS phases for event C have significant lateral variations (Figure 5 and Figure S3, supporting information). There are two prominent sharp changes. First, both the S and SKS travel times are ∼4 s faster at distances between 92.5° and 95° (gray shadowed region in Figure 5). The observed changes occur at the same location for S and SKS indicating that the shallow structures beneath the stations produce this dominant effect. Although the upper mantle shear wave velocity structures beneath western Mediterranean region are not well resolved by global tomography models (Figure 2), if we insert the regional surface wave tomographic model (I. Palomeras et al., Finite-Frequency Rayleigh Wave tomography of the Western Mediterranean, submitted to Geochem. Geophys. Geosyst. 2013) into the global model, we can predict the observed travel time changes very well (Figure S4, supporting information). Note that at the distance of 95° (Figure 5), several stations have ∼2 s early arrivals, which correlate geographically to stations in southern Spain (Figure 4) and are affected by the high-velocity Alboran slab. Although regional tomography models can predict the general trend of travel time decreasing between 92.5° and 95° (Figure S4), the slab images are still not sharp enough to produce the relatively small scale sharp changes we observe. Ideally, we should incorporate the regional high-resolution tomography results to model the absolute travel time of S and

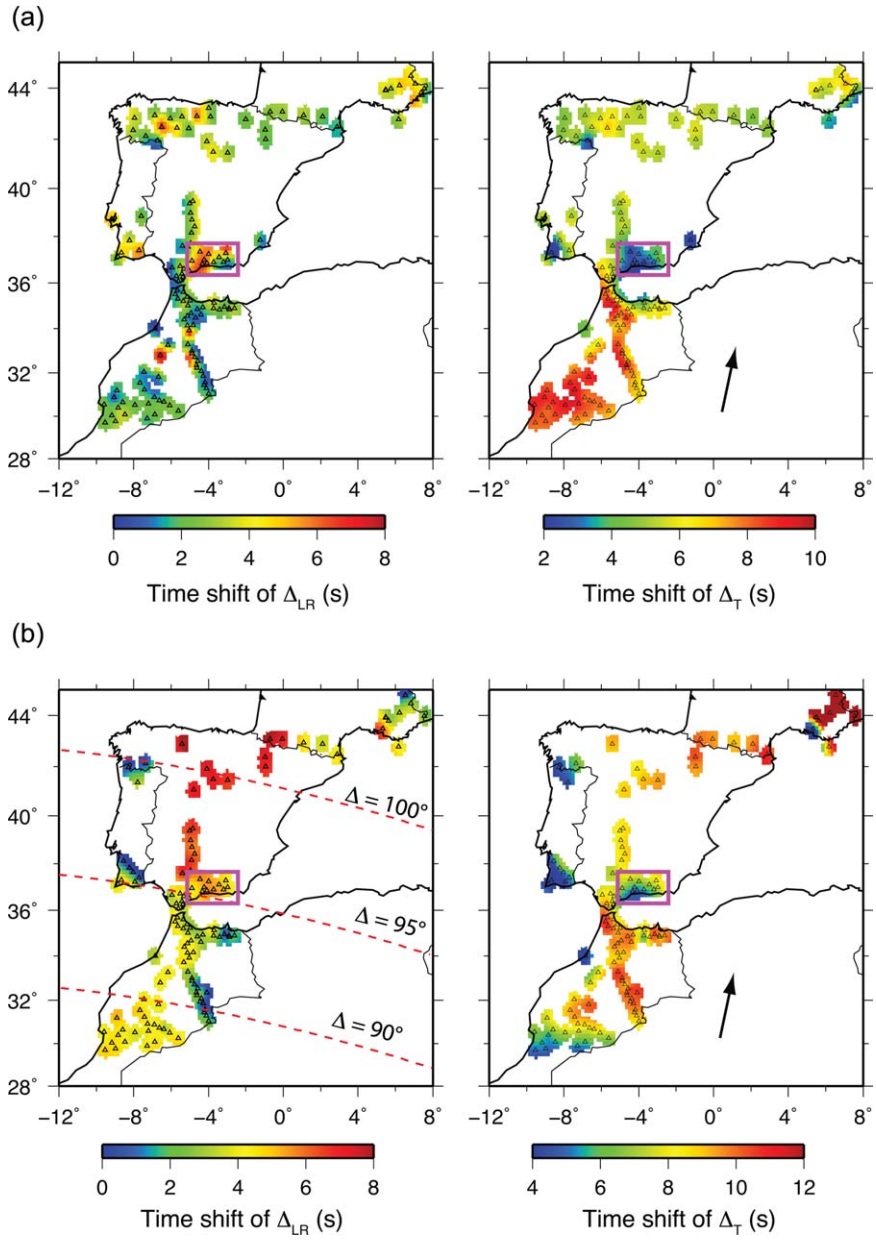


**Figure 4.** MPD patterns for (a) SKS and (b) SV (radial component) for event C from the South Sandwich Islands (Figure 1b). The S phase displays strong multipathing for stations in western Spain (red colors). However, the SKS phase shows no obvious multipathing effects. As shown in Figure 2, the ray paths of SKS and S are nearly identical in the upper mantle, therefore we conclude that the strong multipathing displayed for the S waveforms is caused by structure in the lower mantle. The black arrows indicate the average direction of the ray paths to the array. The magenta rectangles outline the Betics region with large $\Delta_{LR}$ (red color) and delayed $\Delta_T$ for both SKS and SV, which correlates with the subducted Alboran slab in the upper mantle.

SKS. However, regional models covering the whole area beneath the stations, especial those stations at Southern Morocco, are still not available. At this stage, full evaluation of the effects of the shallow structures is difficult, therefore we assume the upper mantle is the same as that in model S40RTS.

[18] The second prominent change observed in Figure 4 is the S travel time. For distances 87.5–90°, the S delay times display a remarkable jump of up to 6 s. In contrast, the SKS travel time delays remain constant at this distance range with large azimuthal variations. *Ritsema et al*. [1998] and *Ni et al*. [1999] observed that S travel times can be

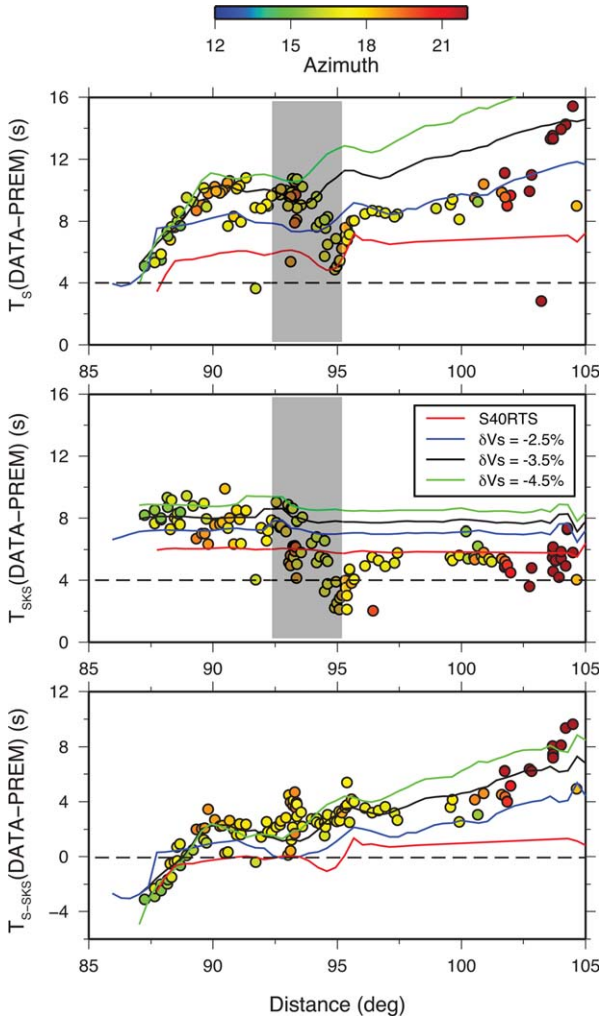


**Figure 5.** Travel times plots. Measurements for S, SKS, and S-SKS differential travel time as compared to the PREM model [*Dziewonski and Anderson*, 1981] for event C. The symbols are color-coded by different azimuths. Red lines indicate the predicted travel times for model S40RTS [*Ritsema et al.*, 2011]. The other colored lines indicate the predicted travel times for models with the same shape as the model SMWA but with different velocity anomalies: blue = −2.5%, black- = −3.5%, and green = −4.5%.

delayed by more than 10 s for events between 65° and 75° as S samples the top of the southern part of the African LLSVP. Our measurements illustrate a much more rapid and isolated occurrence in the S delays, which suggests that the *S* waves approach the top of the northwestern part of African LLSVP at an incidence angle that is more parallel to the structure (Figure 2b). For distances larger than 102°, the S travel time delays display another rapid increase while SKS delays remain relatively small.

[19] To obtain better constraints on the African LLSVP, we emphasize the differential travel time between S and SKS ($T_{S\text{-}SKS}$), as it is mainly controlled by lower mantle structure. Due to the similarity of the ray paths for S and SKS in the upper mantle, $T_{S\text{-}SKS}$ can be used to remove the large scatter in absolute travel time introduced by upper mantle as demonstrated in Figure 5 and Figure S3. Another advantage for using $T_{S\text{-}SKS}$ is that it minimizes the effect from earthquake mislocations. As seen in map view, the travel time variations for stations in Spain and Portugal display more than a ∼4 s increase from the western to eastern stations (Figure 6a). The strong azimuthal behavior of $T_{S\text{-}SKS}$, together with the $\Delta_{LR}$ patterns in Figure 4b, suggests a boundary in the lower mantle. This is also confirmed by the lower mantle tomography models (Figure 6b), although the exact boundaries are not well constrained.

[20] The ScS phases are also important for testing different models for African LLSVP, although the shallow mid-Atlantic Ridge event (event A) has noisy records (Figure 7). For this event, the S ray path samples the midmantle region, which is not affected by the slow African LLSVP (Figure 2). However, the ScS ray path travels directly through the strongest negative part of the LLSVP and should produce significant travel time delays [*Ritsema et al.*, 1998], which is confirmed by the record section shown in Figure 7. The ScS arrivals are delayed up to ∼9 s from the predictions for PREM [*Dziewonski and Anderson*, 1981] (Figure 8). The data also show strong azimuthal variations in ScS. For example, in Figure 7, the two traces at the distance of 73.5° with different azimuths have very different ScS travel times and waveforms, which indicates complex structures exist at the northwestern African LLSVP.

## 4. Modeling

### 4.1. 2-D Modeling

[21] Record sections of the SH components provide important constraints on S phases without SKS phase interference. An example of the stacked SH records for event B is shown in Figure 9 with both (a) S and (b) sS phases. We observe double arrivals on both phases between distances of 86°–90° (shaded region M2), which indicates the existence of a relatively sharp top to the LLSVP. The sharp delays in the S-SKS differential travel times in Figure 5 confirm that the velocity changes from fast to slow across this sharp top with rays sampling deeper into the structure.

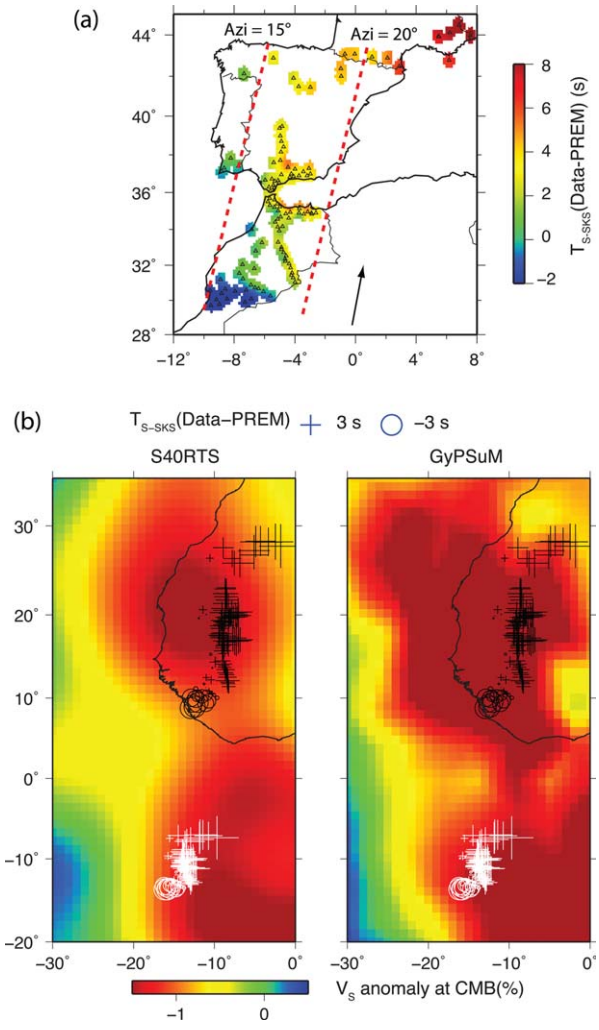


**Figure 6.** (a) The differential time between S and SKS, $T_{S\text{-}SKS}$(Data-PREM), for event C. The abrupt ~4 s jump between the western and eastern stations suggest a velocity boundary. (b) $T_{S\text{-}SKS}$(Data-PREM) values mapped to the SKS piercing points at CMB (black symbols) and S turning points (white symbols) together with the tomography model S40RTS [*Ritsema et al*., 2011] and GyPSuM [*Simmons et al*., 2010] at the base of mantle.

[22] With a sharp top in the model SMWA (Figure 2b), two S arrivals are produced in the synthetics. The first arrival is S, which bottoms in the slow shear wave velocity of the African LLSVP, and then appears as the second arrival at shorter distances. Another phase is produced from the "normal" mantle region above the African LLSVP, which is labeled as phase St (Figure 10). The crossover distance of these two arrivals defines the height of the African LLSVP. Defining the height of the AL1 portion of the model as 600 km, the model SMWA describes the crossover behavior quite well (Figure 9).

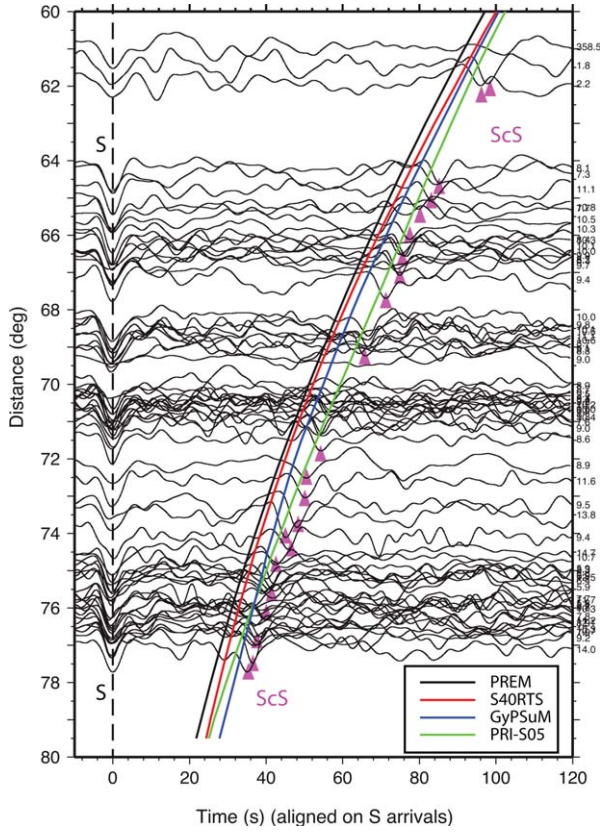


**Figure 7.** Examples of S and ScS record sections for event A. The black, red, blue, and green lines are predicted ScS arrivals for the PREM model, S40RTS [*Ritsema et al*., 2011], GyPSuM [*Simmons et al*., 2010], and PRI-S05 [*Montelli et al*., 2006] respectively. The pink triangles mark examples for ScS arrival. Compared to the predictions of the PREM model, ScS delays up to ~9 s. The numbers on the right side of the plot indicate the azimuths for that trace.

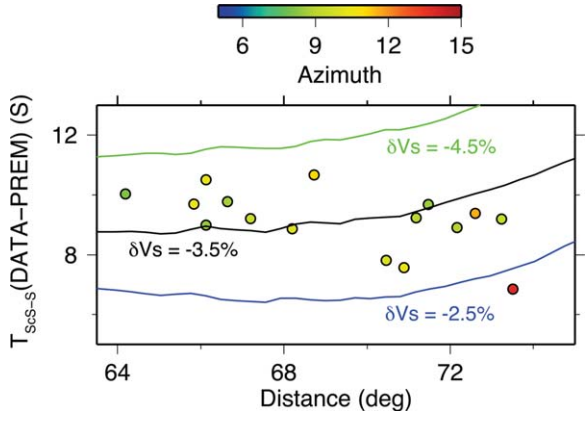


**Figure 8.** The measured ScS-S differential travel times (solid circles) compared to PREM [*Dziewonski and Anderson*, 1981] for event A and the prediction for three models with different velocity anomalies. The different colors of solid circles represent the azimuthal variations and the colored lines are the SMWA model with different velocities: blue = −2.5%, black = −3.5%, and green = −4.5%.

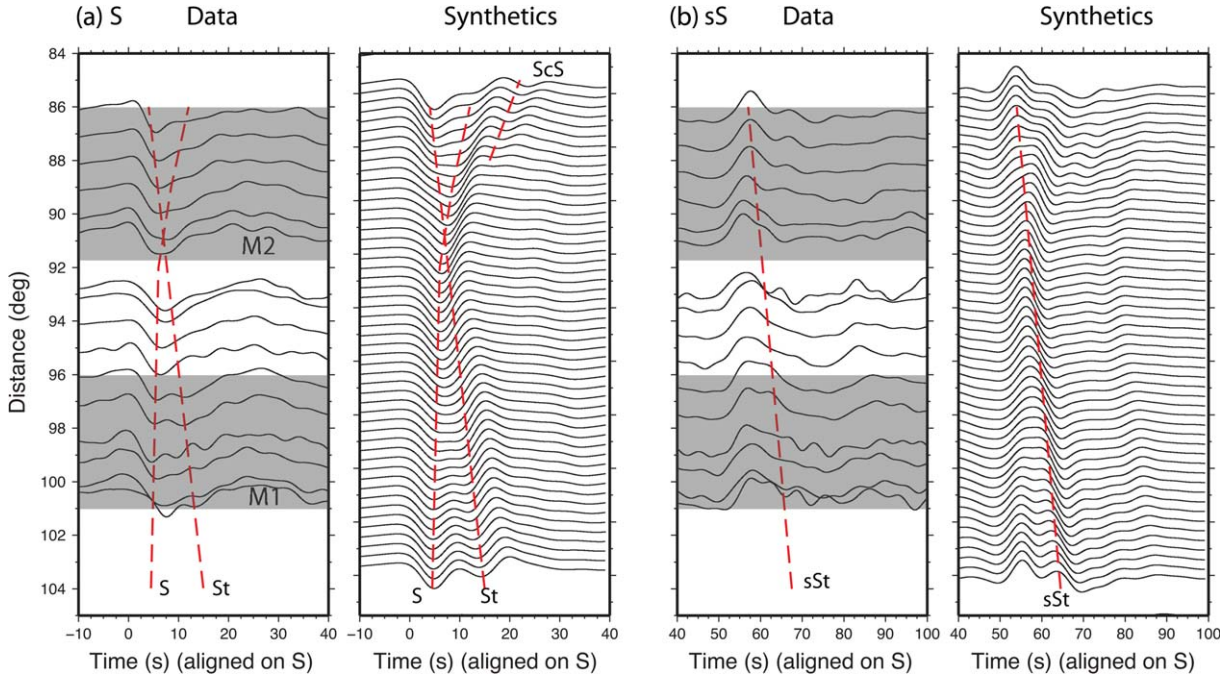


**Figure 9.** Comparison of the (a) SH and (b) sSH data for event B and synthetics using the SMWA model with $\delta$Vs = −3.5%. The data are stacked over 1.5° distance intervals and aligned on the S arrivals. The original data are displayed in Figure S5. The 2-D synthetics reproduce the extra arrivals for phase St, which are caused by multipathing effects when rays pass through the sharp top in the model SMWA. Two gray shaded regions, M1 and M2, emphasize the distance ranges with strongly distorted waveforms and are shown in map view in Figure 3a.

[23] Figure 11 shows an example of SV records for event A illustrating the extra arrivals of the St phase at distances greater than ∼96°, which are predicted by the SMWA model (Figure 11a). For comparison, we also generate synthetics for a hybrid model (Figure 11b), in which velocity perturbations in the bottom 1000 km of S40RTS model are enhanced by a factor of 2. The missing double arrivals on S at larger distances suggest that the top of this hybrid model is not sharp enough to provide significant multipathing effects.

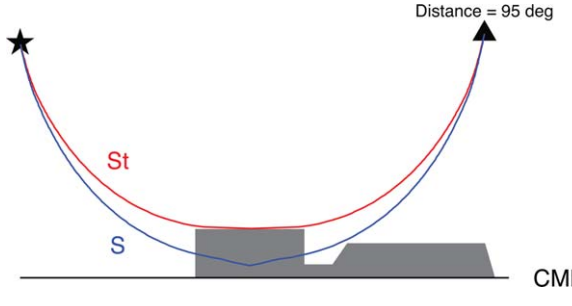


**Figure 10.** Schematic model of ray paths for S and St at a distance of 95°. The gray shaded area represents the model SMWA. The S ray path samples inside of the slow anomaly and the St ray travels through the region at top of the model.

[24] To explain these observed travel times, we apply the same MPD analysis process to the 2-D synthetics to obtain the differential time measurements. We concentrate on $T_{S\text{-}SKS}$ for the azimuth range of 15–20° to avoid the strong azimuthal (3-D) effects produced when the edge of the LLSVP is crossed. The model should be able to predict the two major features observed in travel times. First, the SKS travel time delays appear constant with azimuthal variations along the whole distance when corrected for upper mantle effects (Figure S4). This is also true for the S travel time delays in the distance range of 90–100°. Second, $T_{S\text{-}SKS}$ delays increase sharply for distances between 87.5° and 90°, which are controlled by the delays in S travel times. The model SMWA with shear velocity perturbation of −3.5% predicts the sharp increase of $T_{S\text{-}SKS}$ at small distance. A smaller velocity perturbation model generates much smoother time changing, which is similar to that predicted from the S40RTS model. The model with larger negative velocity perturbations of −4.5% produces much more delayed arrivals for distances between 95° and 100°. However, there is tradeoff between the velocity perturbation and the width of the AL1. For example, if the width of the AL1 is extended, a smaller velocity perturbation

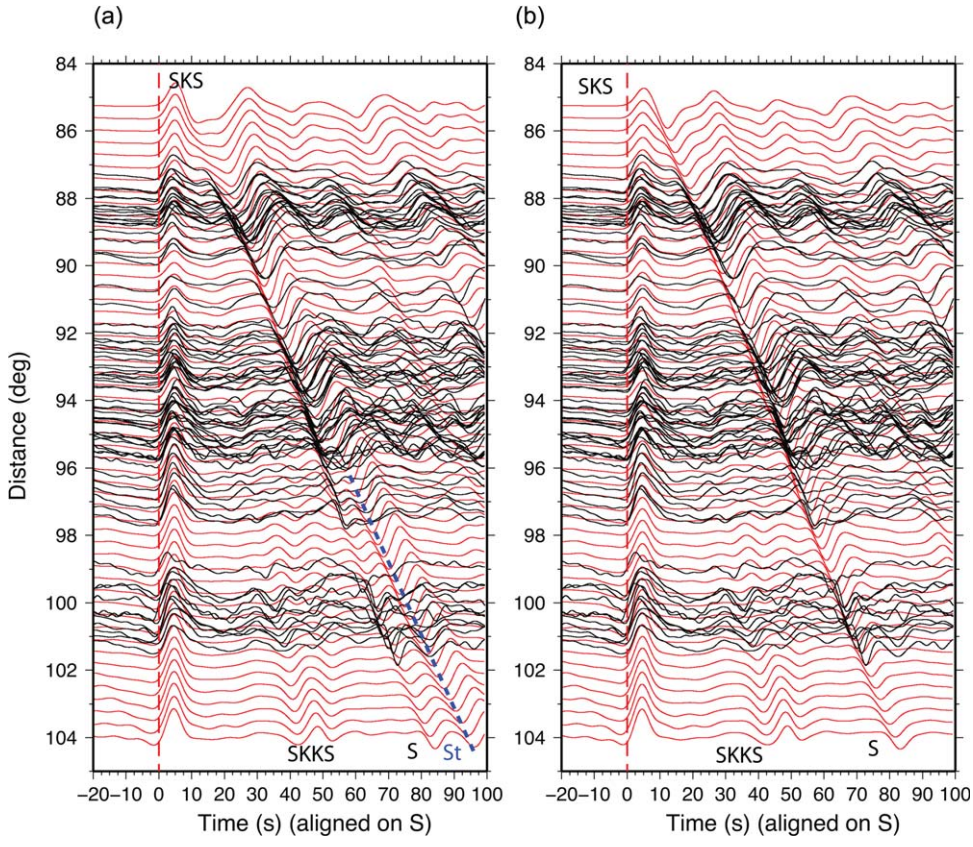


**Figure 11.** Comparison of the observed SV components (black) for event C and synthetics (red) generated by model (a) SMWA with $\delta$Vs = −3.5% and (b) S40RTS with bottom 1000 km enhanced by a factor of two. The model SMWA predicted the extra St arrivals (blue dash lines) as well as the general travel times and waveforms across the whole distance range.

will satisfy the travel delays as well. To resolve this issue, we introduce the ScS phase.

[25] The ScS travel times from event A provide another constraint on the LLSVP properties. Although event A is a shallow event and the waveforms are noisy (Figure 7), we are able to obtain travel times for records with high cross correlation in MPD analysis for both S and ScS. Although the measurements of $T_{ScS-S}$ (Figure 8) have a lot of scatter, they generally have constant travel time values considering the large error in the measurements. Using these additional observations we find that our model SMWA with a fixed 600 km height for AL1 and velocity reduction of −3.5% fits the $T_{ScS-S}$ travel time observations as well (Figure 8).

## 4.2. 3-D Modeling

[26] The multipathing patterns displayed in Figures 3 and 4 and Figure S2 suggest a sharp boundary between the "normal" lower mantle and the African LLSVP (green lines in Figure 12). This sharp edge produces strong 3-D effects, and especially strong azimuthal multipathing as the great circle paths from events to stations are close to the strike of the structure [*Ni et al*., 2005; *To et al*., 2005]. In order to determine whether sharp vertical walls also exist at the northwestern edge of African LLSVP, we use the Spectral Element Method to generate the 3-D synthetics [*Komatitsch et al*., 2002; *Komatitsch and Tromp*, 1999, 2002] and examine their 3-D multipathing patterns.

[27] The 3-D African LLSVP model displayed in Figure 12 is constructed by following the 3-D model developed by *Ni et al*. [2005] and our preferred 2-D model SMWA between azimuth 15° and 20° with a uniform shear velocity perturbation of −3.5%. For depths less than 2100 km, the shear velocity perturbations are the same as in the S40RTS model [*Ritsema et al*., 2011]. We compute 3-D synthetics that are accurate up to 8 s with Specfem3-D Globe (http://geodynamics.org/cig/software/specfem3d-globe). Then, we apply the MPD analysis to the 3-D synthetics and produce the related multipathing maps for event C to

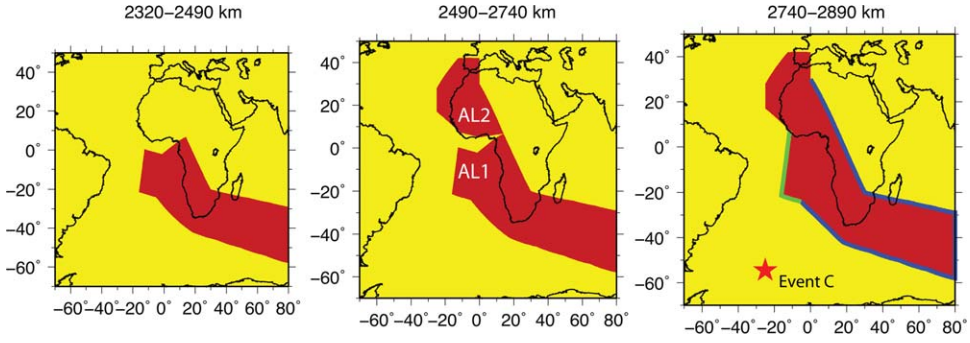


**Figure 12.** 3-D model for African LLSVP at different depths within the lower mantle. Heavy green lines mark the new inferred western and northwestern boundaries from this study. For the southern and eastern boundaries (thick blue lines), we use the position developed by *Ni et al*. [2005] and *Helmberger and Ni* [2005]. We assume a simplified model with uniform 3.5% shear velocity reduction inside (solid red zone). The gap between AL1 and AL2 in the middle plot mimics the gap in the SMWA model as in Figure 2b. The red star shows the location of the South Sandwich Island event (event C) used in this study.

compare to our observations. For comparison, we also low-pass filter the data to 8 s to compare the multipathing patterns more directly (Figure 13a). The 3-D synthetics reproduce the general characteristics of the MPD patterns observed in the data, however there are stronger local variations, which indicate the existence of possible small-scale features within the African LLSVP that are not present in the model. In Figure 13b, we show example waveforms from the 3-D synthetics and data from event C. The predictions from our 3-D model with sharp boundaries predict the azimuthal change observed in the S waveforms successfully, although the synthetics for SKKS do not fit the data well. SKKS rays sample a different region in the lower mantle than S and SKS (Figure 2), which suggests that a more complex internal structure is needed to explain the SKKS data. Fully constraining the northwestern boundaries of the African LLSVP is difficult with the limited distribution of the earthquakes and stations, but our model captures the observed multipathing behaviors in the data S and SKS quite well.

## 5. Model Resolution

[28] Due to the limited data coverage, uncertainties on the geometry and velocity perturbation of the western African LLSVP do exist. For example, the height of AL2 (northeastern region of the LLSVP) is based on the SKS travel times, which can easily be traded off with the velocity inside the structure. Here we assume that both subregions have the same velocity anomaly, which may not be the case.

[29] The slope of the side of the African LLSVP is also important for evaluating different dynamic models. The S ray paths used in this paper are perpendicular to the vertical edge, which indicates our data having limited resolution for determining the slope. In Figure S6 (supporting information), the synthetics seismograms produced by a model with a ~60° dipping edge are almost identical to the synthetics for the vertical wall model. Compared to a tilted top (Figure S7, supporting information), the model with a flat top produces stronger St phase arrivals on both the SH and SV components. We also test models with different topography (aka. roughness) with periodic height variations (Figure S8, supporting information). The strong second arrivals around 85° diminish if the amplitude of the topographic variation is larger than 100 km. This suggests that the top surface of the African LLSVP may have maximum height variations of 100 km. This is also seen in the African LLSVP model developed by *Sun et al*. [2010], which contains an undulating top of approximately 100 km in the vertical. However, the waveform data show large differences (Figure 3a and Figure S5, supporting information), which indicates an azimuthally varying top surface. Another uncertainty is the dimensions of the gap between AL1 and AL2, which is inherited from the S40RTS [*Ritsema et al*., 2011] tomography model (Figure 2). If we remove the gap (Figure S9, supporting information), we can also get a reasonable fit for the data. More stations at shorter distances from the Sandwich Islands would help to resolve this issue by examining the possible abrupt change of SKS arrivals as indicated by model SMWA and could be a direction for future work if data become available.

[30] With those discussed trade-offs, we still obtain a good constraint on the height of the AL1

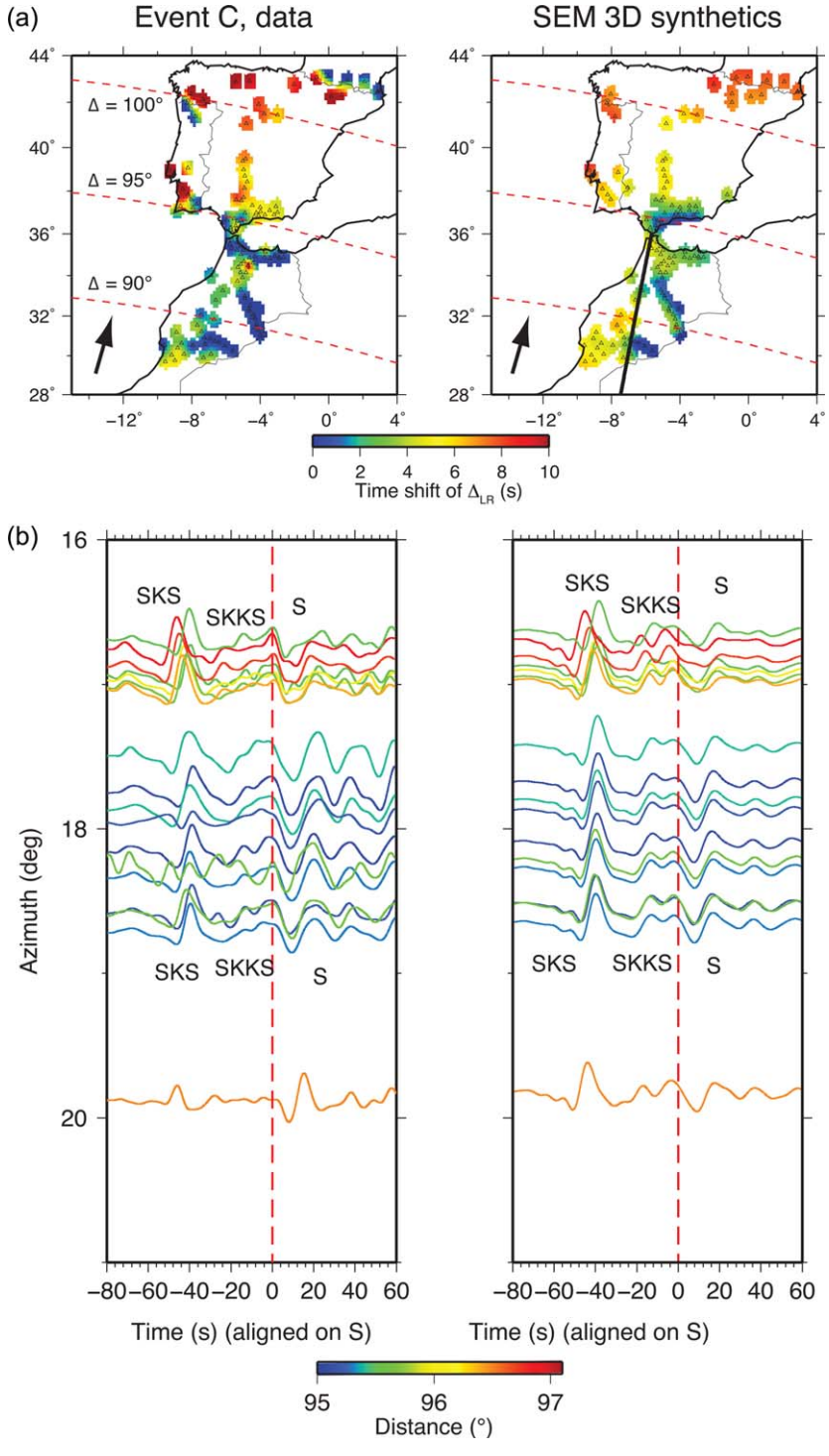


**Figure 13.** Comparison of the data for event C and the 3-D synthetics for the model shown in Figure 12. (a) The MPD patterns for data and 3-D synthetics. (b) Examples of waveforms for (left) data and (right) synthetics at distance range of 95–97°. The waveforms are plotted by azimuth and are aligned on S arrivals as indicated by red dashed lines. The traces in Figure 13b are color-coded by epicentral distance. The 3-D synthetics predict the azimuthal variation at different distances quite well.

region of the western African LLSVP. The 600 km height is characterized by the crossover in the SH waveforms (Figure 9) and the sharp jump in the S travel time (Figure 5). If we elevate the total height by 40 km (Figure 14), the initial distance of the localized change in $T_{S\text{-}SKS}$ is translated to a

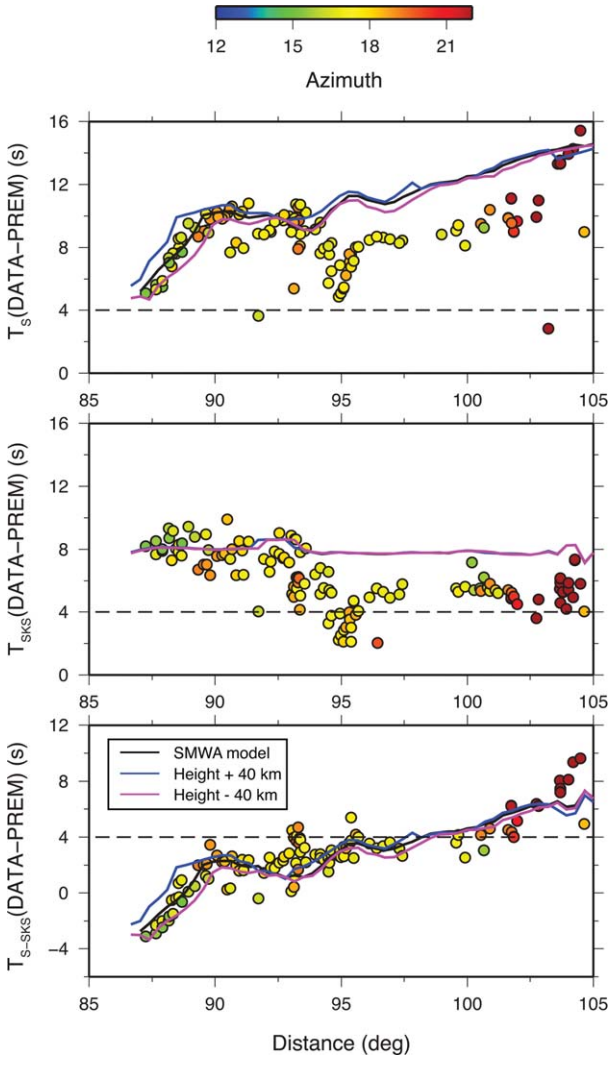


**Figure 14.** Predictions of the travel times for models with different heights of AL1. Measurements for S, SKS, and S-SKS differential travel time as compared to PREM for event C. The symbols are color-coded by different azimuths. Black lines indicate the predicted travel times for model SMWA. Blue lines represent prediction from a model with the height of AL1 elevated by 40 km. Magenta lines are for a model with the height suppressed by 40 km.

shorter distance, which is not in agreement with the observed data. In contrast, the initial distance of the jump in $T_{S\text{-}SKS}$ is translated to a farther distance range if the height is lowered by 40 km.

[31] The northern part of the model, AL2, is also constrained to a height of 400 km above the CMB to satisfy the SKS travel time delays (Figure 5). If the height of AL2 is greater than 400 km, the S travel times are delayed (Figure 2), which is not consistent with the observational data. With a fixed height of AL1, the ScS-S differential times (Figure 8) provide tight constraints on the shear velocity perturbation inside the western African LLSVP (defined as −3.5%). In the model SMWA, we assume the top of the LLSVP is sharp (Figure 15). Modeling tests with a gradational top show that waveforms lose their complexity, which is inconsistent with the observations. For a model with a transitional thickness of 300 km, the St phases are weak, and do not have the same characteristics we find in data (Figure 15c). Therefore, we conclude that the transition thickness of the top of the structure should be less than 200 km but may have considerable lateral variations.

## 6. Discussion and Conclusions

[32] In summary, we have investigated the sharpness of the northwestern African LLSVP by examining the lateral variations observed in S and SKS data recorded by broadband stations in the western Mediterranean. Even with all the uncertainties and trade-offs in parameters, we have robust observations for constraining the structure: (1) the magnitude of the shear velocity anomaly is ∼3.5%; (2) the anomaly extends ∼600 km above the CMB; (3) the top surface of the anomaly is relatively flat; (4) the velocity gradient at the top surface is larger than 3.5% per 200 km. All the observations are consistent with those for the southern and eastern portions of the African LLSVP [*Helmberger and Ni*, 2005; *Wang and Wen*, 2007] and confirmed by lower resolution tomographic models (Figure S1) [*Montelli et al*., 2006; *Ritsema et al*., 2011; *Simmons et al*., 2010].

[33] The gradient of velocity change across the top and side boundaries are useful in distinguishing whether the LLSVP has a pure-thermal or thermochemical origin. *Ni et al*. [2002] concluded that the velocity gradient for the sharp vertical wall should be larger than 3% per 50 km for fitting the anomalous SKS waveforms. *To et al*. [2005] suggested that a gradient of 4.5% over 100 km is needed to explain the observed 3-D effects. Geodynamic models have been developed to satisfy the observed sharp edges by mapping the thermal and chemical anomalies to velocity anomalies. A high-bulk modulus thermodynamic model [*Tan and Gurnis*, 2007] presents a sharp vertical wall with gradient of 3% per 50 km [*Sun et al*., 2007]. In contrast, *Davies et al*. [2012] suggest that the thermal effects may be dominant, and a purely thermal model is adequate to generate sharp velocity gradients of 3–4% per 100 km. However, these models mainly focus on explaining the lateral

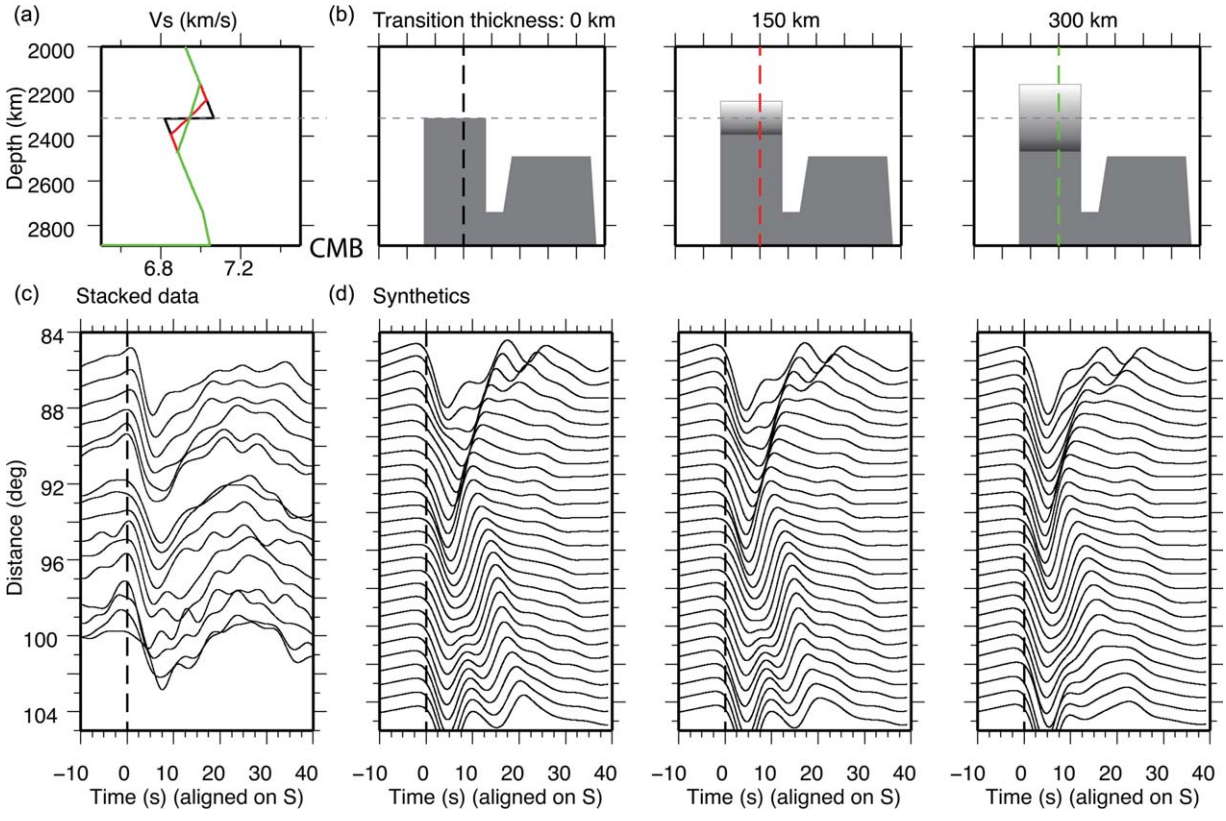


**Figure 15.** Sensitivity tests for models with different transition thicknesses across the top of the model SMWA. (a) The 1-D profiles across three different models. (b) Three representative thicknesses (0, 150, and 300 km) are tested. (c) The data are displayed with (d) synthetics. To produce observed waveforms requires a relatively sharp top with velocity gradient larger than 3.5% per 200 km.

velocity gradient. The velocity gradients across the top of LLSVP are less studied. Here we conclude the top of the western African LLSVP has a velocity gradient larger than 3.5% per 200 km, which is less than those observed for the lateral sharp edges. Dynamic modeling of a LLSVP with a defined top with a gradient of 3% per 150 km to 250 km in the high-bulk modulus thermodynamic model [*Sun et al*., 2007] have also captured these features.

[34] It is worth noting that the large S delays in Figure 5 at distances larger than 102°, correlate to the stations with greater azimuths and sample more of the eastern part of the LLSVP. The large delays indicate that either a higher or slower elevation structure may exist toward the interior of the African LLSVP. Nevertheless, the data suggest that the western portion of the African LLSVP has a continuous high relief across a large area that may connect with the southern portion of the African LLSVP (Figure 12). This large-scale dome-like shape is hard to achieve by a purely thermal model, which generates a more ridge-like structure as shown by *Davies et al*. [2012]. Therefore, a thermal-chemical model is most likely required to satisfy both the sharp edges and large scale of the African LLSVP [*Bower et al*., 2013].

[35] There is a lot of scatter in the S-SKS travel times (Figure 5) and large changes in the waveform data, which indicates that the northwestern African LLSVP is more complex than the southern portion and may be is as complex as the mid-Pacific LLSVP [*He and Wen*, 2012]. A strongly laterally varied top or a jagged lateral boundary as indicated in tomography models [*Montelli et al*., 2006; *Simmons et al*., 2010] may contribute to the observed complexities. However, the limited data make fully understanding the small-scale features difficult. Further, we do not yet have good enough data coverage to provide constraints on the northernmost African LLSVP, specifically how far the northern boundary of the structure extends.

[36] The height of the northwestern African LLSVP is about half that of the southern portion and is close to those observed for central Pacific

LLSVP [*He and Wen*, 2012; *He et al*., 2006]. Recent thermochemical convection models that include plate motions and subduction processes are able to generate more complicated morphology similar to what we observe in both the African and Pacific LLSVPs [*Bower et al*., 2013; *Tan et al*., 2011; *Zhang et al*., 2010]. Nevertheless, better station coverage and further understanding of upper mantle and crust structures will be required to gain complete pictures of these thermochemical piles at the base of the mantle.

## Acknowledgments

[37] The authors would like to thank the Editor Cin-Ty Lee and two anonymous reviewers for their helpful comments. We also thank D. Helmberger and D. Bower for stimulating conversations and constructive reviews. This study was supported by the National Science Foundation, Continental Dynamics Program, under EAR-0809023. This study was also supported by USC postdoctoral scholar research grant. We thank C. Thomas and J. Wookey for sharing their data from the Anti-Atlas, the TopoIberia Project (which provided data from IberArray); and a special thanks to IRIS PASSCAL, C. P. Ryan, M. Harnafi, D. Elouai, and all the people at L'Institut Scientifique at Mohammad V University in Rabat who made the PICASSO experiment possible.

## References

Bezada, M. J., E. D. Humphreys, D. R. Toomey, M. Harnafi, J. M. Davila, and J. Gallart (2013), Evidence for slab rollback in westernmost Mediterranean from improved upper mantle imaging, *Earth Planet. Sci. Lett., 368*, 51–60.

Bower, D. J., M. Gurnis, and M. Seton (2013), Lower mantle structure from paleogeographically constrained dynamic Earth models, *Geochem. Geophys. Geosyst.*, *14*, 44–63. doi:10.1029/2012GC004267.

Chu, R., D. Helmberg, and M. Gurnis (2012), Upper mantle surprises derived from the recent Virginia earthquake waveform data, *Earth Planet. Sci. Lett.*, *14*, 44–63 doi:10.1016/j.epsl.2012.10.023.

Davies, D. R., S. Goes, J. H. Davies, B. S. A. Schuberth, H. P. Bunge, and J. Ritsema (2012), Reconciling dynamic and seismic models of Earth's lower mantle: The dominant role of thermal heterogeneity, *Earth Planet. Sci. Lett.*, *353*, 253–269.

Dziewonski, A. M., and D. L. Anderson (1981), Preliminary reference earth model, *Phys. Earth Planet. Inter.*, *25*(4), 297–356.

Dziewonski, A. M., T. A. Chou, and J. H. Woodhouse (1981), Determination of earthquake source parameters from waveform data for studies of global and regional seismicity, *J. Geophys. Res.*, *86*(B4), 2825–2852.

Grand, S. P. (2002), Mantle shear-wave tomography and the fate of subducted slabs, *Philos. Trans. R. Soc. London A*, *360*(1800), 2475–2491.

He, Y., and L. Wen (2012), Geographic boundary of the ''Pacific Anomaly'' and its geometry and transitional structure in the north, *J. Geophys. Res.*, *117*, B09308, doi:10.1029/2012JB009436.

He, Y. M., L. X. Wen, and T. Y. Zheng (2006), Geographic boundary and shear wave velocity structure of the ''Pacific anomaly'' near the core-mantle boundary beneath western Pacific, *Earth Planet. Sci. Lett.*, *244*(1–2), 302–314.

Helmberger, D. V., and S. Ni (2005), Seismic modeling constraints on the South African Super Plume, in *Earth's Deep Mantle: Structure, Composition, and Evolution, Geophys. Monogr. Ser.*, vol. 160, edited by R. D. van der Hilst, et al., pp. 63–81, AGU, Washington, D. C.

Ishii, M., and J. Tromp (1999), Normal-mode and free-air gravity constraints on lateral variations in velocity and density of Earth's mantle, *Science*, *285*(5431), 1231–1236.

Komatitsch, D., and J. Tromp (1999), Introduction to the spectral element method for three-dimensional seismic wave propagation, *Geophys. J. Int.*, *139*(3), 806–822.

Komatitsch, D., and J. Tromp (2002), Spectral-element simulations of global seismic wave propagation—II. Three-dimensional models, oceans, rotation and self-gravitation, *Geophys. J. Int.*, *150*(1), 303–318.

Komatitsch, D., J. Ritsema, and J. Tromp (2002), The spectral-element method, beowulf computing, and global seismology, *Science*, *298*(5599), 1737–1742.

Liu, L., Y. Tan, D. Sun, M. Chen, and D. Helmberg (2011), Trans-Pacific whole mantle structure, *J. Geophys. Res.*, *116*, B04306, doi:10.1029/2010JB007907.

Marone, F., S. van der Lee, and D. Giardini (2004), Three-dimensional upper-mantle S-velocity model for the Eurasia-Africa plate boundary region, *Geophys. J. Int.*, *158*(1), 109–130.

Masters, G., G. Laske, H. Bolton, and A. Dziewonski (2000), The relative behavior of shear velocity, bulk sound speed, and compressional velocity in the mantle: Implications for chemical and thermal structure, in *Earth's Deep Interior: Mineral Physics and Tomography From the Atomic to the Global Scale, Geophys. Monogr. Ser.*, vol. 117, edited by S. Karato, et al., pp. 63–87, AGU, Washington, D. C.

McNamara, A. K., and S. J. Zhong (2004), Thermochemical structures within a spherical mantle: Superplumes or piles?, *J. Geophys. Res.*, *109*, B07402, doi:10.1029/2003JB002847.

McNamara, A. K., and S. J. Zhong (2005), Thermochemical structures beneath Africa and the Pacific Ocean, *Nature*, *437*(7062), 1136–1139.

Montelli, R., G. Nolet, F. A. Dahlen, and G. Masters (2006), A catalogue of deep mantle plumes: New results from finite-frequency tomography, *Geochem. Geophys. Geosyst.*, *7*, Q11007, doi:10.1029/2006GC001248.

Ni, S. D., and D. V. Helmberger (2003a), Seismological constraints on the South African superplume; could be the oldest distinct structure on Earth, *Earth Planet. Sci. Lett.*, *206*(1-2), 119–131.

Ni, S. D., and D. V. Helmberger (2003b), Ridge-like lower mantle structure beneath South Africa, *J. Geophys. Res.*, *108*(B2), 2094, doi:10.1029/2001JB001545.

Ni, S. D., and D. V. Helmberger (2003c), Further constraints on the African superplume structure, *Phys. Earth Planet. Inter.*, *140*(1-3), 243–251.

Ni, S. D., D. V. Helmberger, and J. Tromp (2005), Three-dimensional structure of the African superplume from waveform modelling, *Geophys. J. Int.*, *161*(2), 283–294.

Ni, S. D., X. M. Ding, D. V. Helmberger, and M. Gurnis (1999), Low-velocity structure beneath Africa from forward modeling, *Earth Planet. Sci. Lett.*, *170*(4), 497–507.

Ni, S. D., E. Tan, M. Gurnis, and D. Helmberger (2002), Sharp sides to the African superplume, *Science*, *296*(5574), 1850–1852.

Ritsema, J., H. J. van Heijst, and J. H. Woodhouse (2004), Global transition zone tomography, *J. Geophys. Res.*, *109*, B02302, doi:10.1029/2003JB002610.

Ritsema, J., S. Ni, D. V. Helmberger, and H. P. Crotwell (1998), Evidence for strong shear velocity reductions and velocity gradients in the lower mantle beneath Africa, *Geophys. Res. Lett.*, *25*(23), 4245–4248.

Ritsema, J., A. Deuss, H. J. van Heijst, and J. H. Woodhouse (2011), S40RTS: A degree-40 shear-velocity model for the mantle from new Rayleigh wave dispersion, teleseismic traveltime and normal-mode splitting function measurements, *Geophys. J. Int.*, *184*(3), 1223–1236.

Simmons, N. A., A. M. Forte, and S. P. Grand (2007), Thermochemical structure and dynamics of the African superplume, *Geophys. Res. Lett.*, *34*, L02301, doi:10.1029/2006GL028009.

Simmons, N. A., A. M. Forte, and S. P. Grand (2009), Joint seismic, geodynamic and mineral physical constraints on three-dimensional mantle heterogeneity: Implications for the relative importance of thermal versus compositional heterogeneity, *Geophys. J. Int.*, *177*(3), 1284–1304.

Simmons, N. A., A. M. Forte, L. Boschi, and S. P. Grand (2010), GyPSuM: A joint tomographic model of mantle density and seismic wave speeds, *J. Geophys. Res.*, *115*, B12310, doi:10.1029/2010JB007631.

Su, W. J., and A. M. Dziewonski (1997), Simultaneous inversion for 3-D variations in shear and bulk velocity in the mantle, *Phys. Earth Planet. Inter.*, *100*(1-4), 135–156.

Sun, D., and D. Helmberger (2011), Upper-mantle structures beneath USArray derived from waveform complexity, *Geophys. J. Int.*, *184*(1), 416–438.

Sun, D., E. Tan, D. Helmberger, and M. Gurnis (2007), Seismological support for the metastable superplume model, sharp features, and phase changes within the lower mantle, *Proc. Natl. Acad. Sci. U. S. A.*, *104*(22), 9151–9155.

Sun, D., D. Helmberger, S. Ni, and D. Bower (2009), Direct measures of lateral velocity variation in the deep earth, *J. Geophys. Res.*, *114*, B05303, doi:10.1029/2008JB005873.

Sun, D., D. Helmberger, and M. Gurnis (2010), A narrow, mid-mantle plume below southern Africa, *Geophys. Res. Lett.*, *37*, L09302, doi:10.1029/2009GL042339.

Tackley, P. J. (2012), Dynamics and evolution of the deep mantle resulting from thermal, chemical, phase and melting effects, *Earth Sci. Rev.*, *110*(1-4), 1–25.

Tan, E., and M. Gurnis (2005), Metastable superplumes and mantle compressibility, *Geophys. Res. Lett.*, *32*, L20307, doi:10.21029/2005GL024190.

Tan, E., and M. Gurnis (2007), Compressible thermochemical convection and application to lower mantle structures, *J. Geophys. Res.*, *112*, B06304, doi:10.1029/2006JB004505.

Tan, E., W. Leng, S. Zhong, and M. Gurnis (2011), On the location of plumes and lateral movement of thermochemical structures with high bulk modulus in the 3-D compressible mantle, *Geochem. Geophys. Geosyst.*, *12*, Q07005, doi:10.01029/2011GC003665.

To, A., B. Romanowicz, Y. Capdeville, and N. Takeuchi (2005), 3D effects of sharp boundaries at the borders of the African and Pacific Superplumes: Observation and modeling, *Earth Planet. Sci. Lett.*, *233*(1-2), 137–153.

Wang, Y., and L. X. Wen (2007), Geometry and P and S velocity structure of the ''African Anomaly'', *J. Geophys. Res.*, *112*, B05313, doi:10.1029/2006JB004483.

Yang, Y. J., M. H. Ritzwoller, A. L. Levshin, and N. M. Shapiro (2007), Ambient noise rayleigh wave tomography across Europe, *Geophys. J. Int.*, *168*(1), 259–274.

Zhang, N., S. Zhong, W. Leng, and Z. X. Li (2010), A model for the evolution of the Earth's mantle structure since the Early Paleozoic, *J. Geophys. Res.*, *115*, B06401, doi:10.1029/2009JB006896.

Zhu, H., E. Bozdag, D. Peter, and J. Tromp (2012), Structure of the European upper mantle revealed by adjoint tomography, *Nat. Geosci.*, *5*(7), 493–498.